Multiscale Simulation of a Prescribed Fire Event in the New Jersey Pine Barrens Using ARPS-CANOPY

MICHAEL T. KIEFER,* WARREN E. HEILMAN,+ SHIYUAN ZHONG,* JOSEPH J. CHARNEY,+ XINDI BIAN,+ NICHOLAS S. SKOWRONSKI,# JOHN L. HOM,@ KENNETH L. CLARK,& MATTHEW PATTERSON,@ AND MICHAEL R. GALLAGHER&

* *Department of Geography, Michigan State University, East Lansing, Michigan*
+ *Northern Research Station, USDA Forest Service, East Lansing, Michigan*
# *Northern Research Station, USDA Forest Service, Morgantown, West Virginia*
@ *Northern Research Station, USDA Forest Service, Newtown Square, Pennsylvania*
& *Northern Research Station, USDA Forest Service, New Lisbon, New Jersey*

(Manuscript received 12 April 2013, in final form 16 September 2013)

ABSTRACT

Smoke prediction products are one of the tools used by land management personnel for decision making regarding prescribed fires. This study documents the application to a prescribed fire of a smoke prediction system that employs ARPS-CANOPY, a modified version of the Advanced Regional Prediction System (ARPS) model containing a canopy submodel, as the meteorological driver. In this paper, the performance of ARPS-CANOPY in simulating meteorological fields in the vicinity of a low-intensity fire is assessed using flux-tower data collected prior to and during a low-intensity prescribed fire in the New Jersey Pine Barrens in March 2011. A three-dimensional high-resolution plant area density dataset is utilized to define the characteristics of the canopy, and the fire is represented in ARPS-CANOPY as a heat flux to the atmosphere. The standard ARPS model is compared with reanalysis and upper-air data to establish that the model can simulate the observed synoptic-mesoscale and planetary boundary layer features that are salient to this study. ARPS-CANOPY profiles of mean turbulent kinetic energy, wind speed/direction, and temperature exhibit patterns that appear in the flux-tower observations during both the preburn phase of the experiment and the period of time the flux tower experienced perturbed atmospheric conditions due to the impinging fire. Last, the character and source of turbulence in and around the fire line are examined. These results are encouraging for smoke prediction efforts since transport of smoke from low-intensity fires is highly sensitive to the near-surface meteorological conditions and, in particular, turbulent flows.

1. Introduction

Prescribed fire is a tool used by public and private land managers to accomplish forest and agricultural land management goals. Between 1998 and 2011, more than 184 000 prescribed fires were conducted in the United States with more than 300 million acres of land burned (National Interagency Fire Center 2012), and an estimated 20.2 million acres of land were treated with prescribed fire in 2011 alone (Melvin 2012). In contrast to wildfires, which often threaten natural resources, property, and human life, prescribed fires in the eastern United States are typically of lower intensity, confined to smaller areas, and rarely pose a direct threat of damage to surrounding communities. Note that prescribed fires can vary in intensity and size considerably and that fire intensity can be measured using a number of different metrics [e.g., heat flux, duration of heating, radiant energy; Keeley (2009)]. However, smoke from prescribed fires can affect public health and safety in nearby communities, as well as the health and safety of operational fire management personnel, mainly through air quality and visibility degradation. Because air quality and visibility issues occur more often when smoke concentrations are large, smoke prediction products (e.g., particle concentration forecasts) are an important component of the suite of tools used by land management personnel for decision making regarding planned burns.

The prediction of local smoke dispersion from low-intensity fires is made challenging by the influence of

Corresponding author address: Michael Kiefer, Michigan State University, Geography Bldg. Rm. 203, 673 Auditorium Rd., East Lansing, MI 48824.
E-mail: mtkiefer@msu.edu

DOI: 10.1175/JAMC-D-13-0131.1

a number of interrelated factors, including near-surface meteorological conditions, local topography, vegetation structure, and atmospheric turbulence within and above vegetation layers. A broad goal of this study is to build a smoke management tool specifically for low-intensity prescribed fires by taking advantage of state-of-the-science finescale atmospheric dispersion models. While smoke dispersion models have been developed and applied to wildland fires, a number of factors limit their applicability to local smoke dispersion episodes associated with prescribed fires. Dispersion models [e.g., Simple Approach Smoke Estimation Model (SASEM; Riebau et al. 1988); VSMOKE (Lavdas 1996)] are typically location specific and are often limited by the simplifying assumptions they employ to account for emissions source, topography, canopy, and the atmospheric conditions. Furthermore, while integrated smoke dispersion modeling systems [e.g., BlueSky (Larkin et al. 2009)] have been developed for the prediction of smoke from multiple sources on a regional scale, they are unable to resolve the processes necessary to simulate the local dispersion of smoke from low-intensity fires. None of the aforementioned modeling systems are suitable for low-intensity fires wherein smoke may meander around the source and reside within forest canopies for an extended period of time.

The work detailed herein is part of a broader study to develop a new smoke dispersion prediction system specifically designed for application to prescribed fires, and a key component of such a system is a meteorological driver. The meteorological model chosen for this purpose is the Advanced Regional Prediction System (ARPS; Xue et al. 2000, 2001). ARPS is designed to simulate atmospheric flows from the microscale to the synoptic scale, making it particularly useful for the transport of smoke across multiple scales. It is worth noting that ARPS has been applied to the prediction of scalar transport and dispersion (Michioka and Chow 2008). In their study, dispersion from a nonbuoyant point source was simulated using a series of nested one-way grids with horizontal grid spacing varying from 45 km to 25 m. Note that although a passive scalar equation was added to ARPS by Michioka and Chow (2008) to simulate the transport and dispersion of tracer gases, such an equation is of limited use for the prediction of smoke from fires due to the presence of highly buoyant particles from the fire.

Whereas it is possible to simulate the dispersion of smoke using simplified dispersion parameterizations, use of a model such as ARPS that can simulate mean flow and resolve some scales of turbulent motion allows one to evaluate atmospheric processes that affect both smoke dispersion within a forest canopy and the possible transport of smoke through the canopy–atmosphere interface and into the planetary boundary layer. As a point of clarification, a canopy is defined within the context of this study as the entire vegetation layer, including the crown. Although there are aspects of ARPS that make it a suitable model for the current application (e.g., extensively validated, multiscale capability), the standard ARPS formulation lacks the capability to explicitly simulate atmospheric variables (e.g., wind velocity, temperature) inside a multiple grid-level canopy. Within the ARPS framework, as with many mesoscale models, the bulk effect of a vegetation canopy on the atmosphere is computed within a single layer, beneath the lowest model grid point. A modified version of ARPS, termed ARPS-CANOPY, has been developed by Kiefer et al. (2013) to allow for simulation of airflow within a vegetation canopy, the salient aspects of which are described in section 2a.

In this paper, we assess the ability of the model to represent the micrometeorology in the vicinity of instrumented flux towers on two days: one in which a low-intensity burn was conducted and another in which no fire activity occurred. We choose to focus on the near-surface micrometeorology in this study, and leave analysis of the smoke dispersion component of the prediction system to future work. While the performance of ARPS-CANOPY has been evaluated in a nonfire environment by Kiefer et al. (2013) using Canopy Horizontal Array Turbulence Study (CHATS) experiment (Patton et al. 2011) data from a walnut orchard, the application of the model to a fire environment is a necessary step in the model development process. To achieve this goal, we evaluate the performance of ARPS-CANOPY with meteorological data collected prior to and during a low-intensity prescribed fire conducted in the New Jersey Pine Barrens in March 2011, hereinafter referred to as the Butler Place fire (see section 3a for more details). A series of one-way nested grid simulations are performed, centered on the burn location, in which standard ARPS is utilized for all grids except for the innermost domain, where ARPS-CANOPY is applied. In ARPS-CANOPY, the finescale combustion process is parameterized as a heat source on the resolved model grid, and the progression of the fire line is represented by a simplified evolution. Although our primary goal is to evaluate the simulated micrometeorology in and above the canopy, the multiscale modeling approach we employ in this study allows us to examine scales of atmospheric motion ranging from synoptic to microscale.

The remainder of this paper is organized as follows. A description of the ARPS-CANOPY model and how it differs from the standard ARPS model is presented in section 2a, followed by a description of the model

configuration and parameterization in section 2b. A brief summary of the Butler Place fire is provided in section 3a, along with a description of the vegetation dataset derived using an airborne lidar in section 3b, and a review of the fire parameterization in ARPS-CANOPY in section 3c. Results from the case study simulations including a synoptic-mesoscale overview are presented in section 4a and preburn and burn day model evaluations are shown in section 4b. The paper is concluded in section 5.

2. Model description and numerical design

a. *ARPS-CANOPY overview*

ARPS is a three-dimensional, compressible, nonhydrostatic atmospheric model with a terrain-following coordinate system. ARPS is capable of multiscale simulations, with the model having been applied with grid spacing as fine as $O(1\,\text{m})$ by Dupont and Brunet (2008, 2009), while having also been applied with much coarser grid spacing of $O(1\text{–}10\,\text{km})$ to mesoscale and synoptic-scale phenomena (e.g., Xue et al. 2003; Parker and Johnson 2004; Michioka and Chow 2008).

A modified version of ARPS was developed by Kiefer et al. (2013), based on earlier modifications made by Dupont and Brunet (2008), to account for the effects of vegetation elements on flow through a vegetation canopy. A brief overview of the modifications made follows here; for more details, see Kiefer et al. (2013). Following Dupont and Brunet (2008), a term was added to the momentum equation to account for drag that occurs due to the presence of the canopy elements, and a term was added to the subgrid-scale (SGS) turbulent kinetic energy (TKE) equation to account for the enhancement of turbulence dissipation in the canopy air space. Following Kanda and Hino (1994), a production term was also added to the SGS TKE equation to represent the production of SGS TKE in the wakes of canopy elements, at scales large enough that the turbulence does not dissipate immediately yet small enough that it remains unresolved. To account for the impact of the canopy elements on heating/cooling processes inside the canopy layer and net radiation at the ground surface, changes to the ARPS radiation parameterization were made following the work by Sun et al. (2006a). First, a set of equations was added to the radiation physics module to compute the net radiation flux at canopy top and a profile of net radiation was prescribed that assumes an approximately exponential decay within the canopy. Second, a term was added to the thermodynamic equation to represent heating (cooling) of the canopy air spaces that results from the vertical flux convergence (divergence) of net radiation absorbed by the canopy elements. Last, the magnitude of the ground net radiation flux was reduced, by a factor proportional to the density of the canopy, to account for shading by the overlying vegetation during the day and reduction of longwave ground radiation at night.

In Kiefer et al. (2013), ARPS-CANOPY was used to simulate the mean and turbulent flow observed on two days during the CHATS experiment: one in late March when the trees were dormant without leaves and another in late May when the trees were full of mature leaves. In both cases, the vertical profiles of simulated mean wind, temperature, and TKE in and above the canopy were shown to be in qualitative agreement with the observations, with errors smallest in the afternoon and in the case with stronger mean wind speed. Furthermore, sensitivity experiments with 90-m horizontal grid spacing retained the profile shapes and diurnal trends seen in simulations with 30-m horizontal grid spacing.

We emphasize here that ARPS-CANOPY does not resolve the flow around individual trees or the heating/cooling of individual branches or leaves. From canopy drag and turbulence production to canopy shading and heating/cooling of the canopy air space, the canopy is represented in the model as a height-varying plant area density profile (A_p), specified at each grid point. The quantity A_p, defined as the one-sided area of all plant material per unit volume of canopy, is a bulk measure of the vegetation element density averaged across multiple trees [for the grid spacing used in this study, $O(100)$ trees]. The development of an A_p dataset derived from airborne lidar measurements will be discussed later in section 3b.

b. *Model configuration and parameterization*

A series of one-way nested simulations are performed using ARPS/ARPS-CANOPY, with horizontal grid spacing ranging from 8.1 km in the outermost grid to 100 m in the innermost grid (Fig. 1 and Table 1). As shown in Fig. 1, the outermost domain (domain 1) covers the northeastern United States, while the innermost domain (domain 5) covers only the area within several kilometers of the Butler Place burn (see star in Fig. 1b). A distinction needs to be made here between domains 1–4, in which the standard ARPS model is employed, and domain 5, in which ARPS-CANOPY is applied. Also, note that the fire is only introduced in domain 5 (see section 3c). As mentioned earlier, the multiscale modeling strategy utilized in this study allows us to examine a range of atmospheric scales of motion, from synoptic to mesoscale to microscale. As a consequence of this one-way nesting strategy, domains 1–4 simulate synoptic- to mesoscale processes and provide boundary

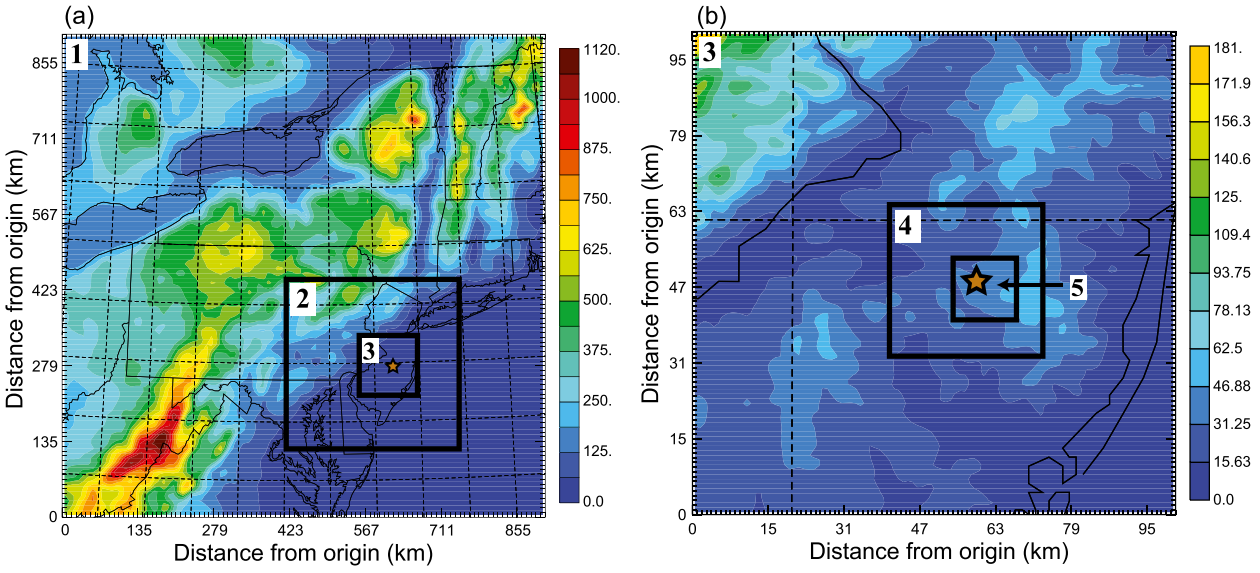

FIG. 1. Maps of surface elevation (m) from (a) domain 1 overlaid with outlines of domains 2 and 3 and (b) domain 3 overlaid with outlines of domains 4 and 5. The star in domain 5 indicates the approximate location of the Butler Place burn.

conditions for domain 5, the domain with the canopy submodel and fire, but domains 1–4 do not simulate fire or resolve in-canopy flows (although the transfer of momentum and scalars between the atmosphere and a vegetation–soil layer is accounted for in standard ARPS). Such a modeling strategy is dependent on the assumption that the heat output from a small, low-intensity fire has a negligible impact on the bulk properties of the planetary boundary layer (e.g., PBL height, mean wind speed), outside of the immediate vicinity of the fire. A similar assumption is made regarding the sensitivity of the PBL to intracanopy momentum and heat transport.

Initial and lateral boundary conditions are supplied to the outermost grid from the North American Regional Reanalysis (NARR; Mesinger et al. 2006), while the upper boundary condition for all simulations is a sponge layer in the upper 2 km of the domain. Terrain data for domains 1–3 are generated from 30-arc-s-resolution U.S. Geological Survey (USGS) datasets and for domains 4 and 5 from 3-arc-s-resolution USGS datasets. Land-use data for the outer four domains are generated from 1-km-resolution USGS land-use data, while for the innermost domain, the land use is heterogeneous forest, defined at each grid point with a vertical profile of plant area density obtained from lidar observations (see section 3b for description of methodology). For domains 1–4, all simulations are initialized at 2000 eastern daylight time (EDT; UTC − 4 h) 18 March 2011 and run for 60 h to end at 0800 EDT 21 March 2011; for domain 5, two 12-h simulations are run, the first initialized at 0800 EDT 19 March (preburn day) and the second at 0800 EDT 20 March (burn day). Also, the 20 March simulation is repeated without the fire parameterization (termed no-fire simulation), to examine the impact of the strong heat source on the mean and turbulent flow.

For all five domains, a 1.5-order subgrid-scale turbulence closure scheme with a prognostic equation for TKE is utilized (Moeng and Wyngaard 1989), as well as a land surface model based on Noilhan and Planton (1989) and Pleim and Xiu (1995), and radiation physics following Chou (1990, 1992) and Chou and Suarez (1994) (however with computation of the canopy heat source term and attenuation of net radiation inside the canopy applied, as discussed in section 2a). Effects of

TABLE 1. Nested grid configurations with dimensions.

Domain	Grid size	Domain (km)	Δx, Δy	Δz_{min} (m)
1	115 × 115 × 53	907.2 × 907.2 × 16.0	8.1 km, 8.1 km	50
2	115 × 115 × 53	302.4 × 302.4 × 16.0	2.7 km, 2.7 km	40
3	115 × 115 × 63	100.8 × 100.8 × 15.9	900 m, 900 m	40
4	103 × 103 × 73	30.0 × 30.0 × 15.8	300 m, 300 m	20
5	103 × 103 × 83	10.0 × 10.0 × 12.0	100 m, 100 m	2

TABLE 2. Physics parameterization summary. Note that Lin et al. refers to Lin et al. (1983) and Kain–Fritsch refers to Kain and Fritsch (1993). For domains 1–4, the nonlocal turbulence scheme available in ARPS, based on Sun and Chang (1986) is utilized in addition to the SGS 1.5-order TKE scheme. For domain 5, moisture is treated as a passive scalar (i.e., no phase changes) since ARPS-CANOPY is unable at this time to treat moisture transport through the canopy.

Domain	Microphysics	Convective parameterization scheme	ARPS–ARPS-CANOPY	Fire?
1	Lin et al.	Kain–Fritsch	ARPS	No
2	Lin et al.	None	ARPS	No
3	Lin et al.	None	ARPS	No
4	Lin et al.	None	ARPS	No
5	None	None	ARPS-CANOPY	Yes

topographic shading on radiative fluxes are accounted for as in Colette et al. (2003). With the exception of the innermost grid, the size of the grid cells dictates that nonlocal turbulent mixing be parameterized, which is achieved in ARPS by using an ensemble turbulence closure scheme based on Sun and Chang (1986), in addition to the 1.5-order subgrid-scale (local) turbulence scheme. For all domains, fourth-order-accurate finite differencing of the advection terms is used in both the vertical and horizontal directions. A summary of the physics parameterization options for each nested grid is provided below (see Table 2). Note that for domain 5, moisture is treated as a passive scalar (i.e., no phase changes) since ARPS-CANOPY is unable at this time to treat moisture transport through the canopy. The development of a moisture transport module is planned as part of future upgrades to ARPS-CANOPY.

3. Experimental data and modeling implementation

a. *Fire experiment*

The Butler Place field experiment was conducted in order to collect meteorological and air quality data prior to, during, and following a low-intensity prescribed fire. The prescribed fire was conducted by the New Jersey Forest Fire Service as part of a seasonal program of operational burns in the New Jersey Pine Barrens. The burn unit was approximately 265 acres in size, with overstory vegetation consisting of pitch pine (*Pinus rigida* Mill.) and mixed oak (*Quercus* spp.); understory vegetation consisting of blueberry (*Vaccinium* spp.), huckleberry (*Gaylussacia* spp.), and scrub oaks; and a litter layer consisting of pine needles, shrub foliage, and 1-, 10-, and 100-h woody fuels. Continuous measurements were taken beginning at 0100 EDT 19 March 2011 and continuing until approximately 0800 EDT 21 March. Three instrumented towers of 10-, 20-, and 30-m heights were located inside the burn unit, with a second 10-m-tall tower located approximately 1 km northwest of the burn unit (Fig. 2). Additionally, twelve 3-m-tall towers were deployed to sample air temperature and smoke inside the burn unit, and four monitors of particulate matter smaller in diameter than 2.5 μm ($PM_{2.5}$) were arranged around the perimeter of the burn and at locations downwind of the burn unit (not shown).

Although a variety of meteorological and air quality instrumentation was employed during the experiment, we restrict our discussion to the instrumentation on the 20- and 30-m towers, as only data from those towers are utilized in this study. Both towers were instrumented with sonic anemometers, temperature–relative humidity probes, and thermocouples, as well as carbon monoxide (CO) and carbon dioxide (CO_2) sensors, barometers, and soil thermocouples. Additionally, the 20-m tower was equipped with a radiative heat flux sensor (Medtherm 64-20-20) at the 4.5-m level, and the 30-m tower was equipped with a net radiometer (Kipp and Zonen NR-Lite) at the 30-m level. A summary of the instrumentation most relevant to this model assessment work (sonic anemometers, temperature probes, and thermocouples) is provided in Table 3. For a detailed description of the field experiment, including additional instrumentation not described in this paper, see Heilman et al. (2013).

While a complete description of the Butler Place ignition strategy and fire-line evolution is beyond the scope of this study, a summary of the salient aspects is provided here. Ignition via hand-held drip torch began in the extreme southwest area of the burn unit at 0955 EDT 20 March, with ignition efforts proceeding eastward and northward for the next 9.5 h, following a series of west–east- and north–south-oriented plowed control lines, until approximately 1930 EDT. A light northeasterly wind veered to the southeast during the burn period, and the fire propagated slowly to the northeast at an average speed of about 1.5 m min^{-1} (estimated). The fire line passed the 20-m tower at 1520 EDT and the 30-m tower at 1823 EDT; note that partial mechanical

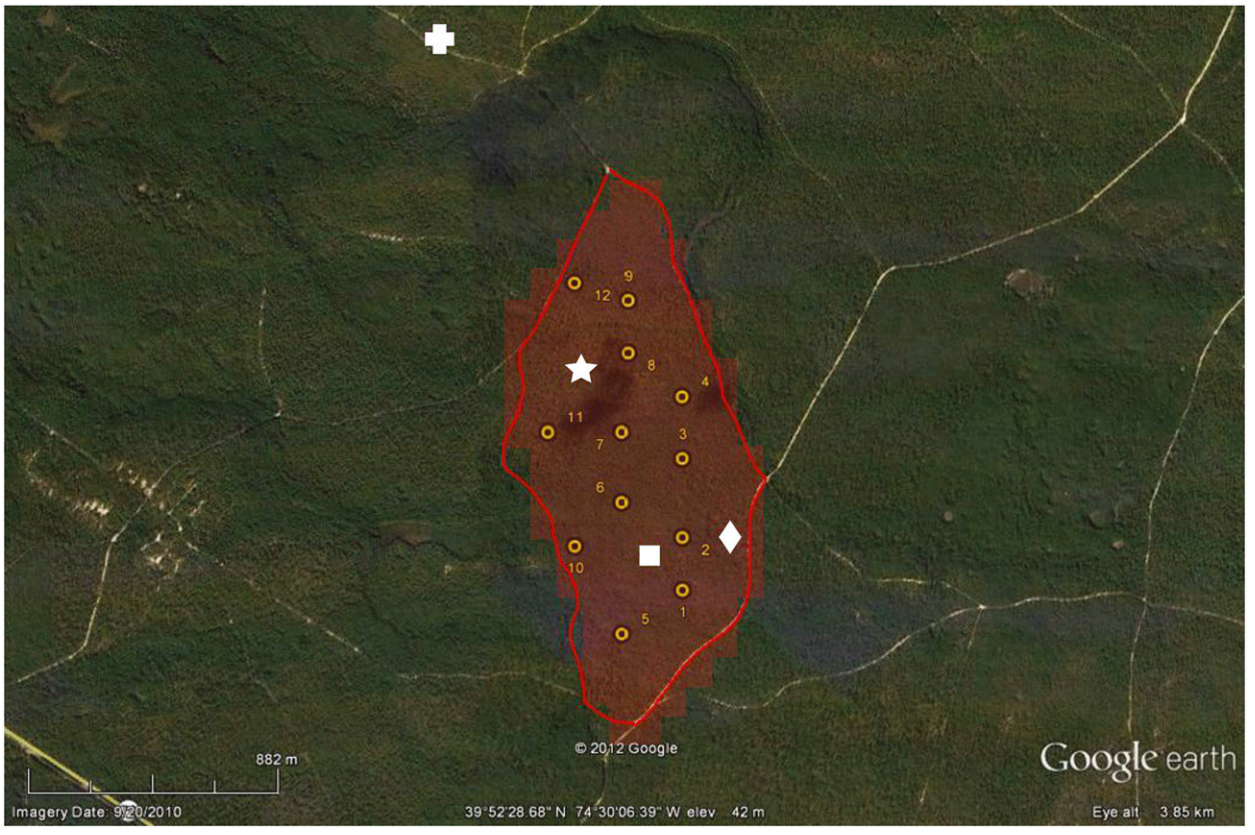

FIG. 2. Aerial image of burn unit outlined in red overlaid with circles depicting locations of the control tower (plus sign), 10-m tower (star), 20-m tower (square), and 30-m tower (diamond). The yellow circles denote the locations of the twelve 3-m towers. The outline of the ARPS-CANOPY representation of the burn unit is in transparent red shading.

removal of fuels was conducted prior to the burn within a 5–7-m radius of each tower to minimize the potential damage to instrumentation. The entire burn was completed in approximately 16 h.

b. *Forest canopy dataset*

As discussed in section 2a, the vegetation canopy is represented in ARPS-CANOPY as a height-varying plant area density profile specified at each grid point. Whereas the meaningful estimation of A_p is challenging at even the scale of single tree stands, it has been demonstrated that lidar-derived canopy height profiles (CHPs) can be utilized to characterize the three-dimensional canopy structure (e.g., canopy bulk density, kg m^{-3}) at high horizontal and vertical resolutions on spatial scales O (10 km) (Skowronski et al. 2011). Here, we have estimated A_p on a grid with 100-m (horizontal) and 2-m (vertical) grid spacing for use with domain 5 (Fig. 1b) through an integration of multiple airborne laser scanning (ALS) datasets and field-based destructive sampling. We

TABLE 3. Summary of selected instrumentation and monitoring protocols used at the 20- and 30-m towers during the prescribed fire experiment. Here, u, v, and w refer to the three Cartesian wind components, T is temperature, and RH is relative humidity. See Heilman et al. (2013) for a full summary.

Tower height (m)	Instrument	Variable	Measurement height (m AGL)	Sampling frequency (Hz)
20	3D sonic anemometers (R. M. Young 81000V)	u, v, w, T	3, 10, 20	10
20	Temperature–RH probes (Vaisala HMP50)	Mean T, RH	3, 10, 20	10
20	Thermocouples (Omega SSRTC-GG-K-36–36)	T	0, 1, 2, 3, . . . , 10, 12.5, 15, 17.5, 20	10
30	3D sonic anemometers (R. M. Young 81000V)	u, v, w, T	3, 10, 30	10
30	Temperature–RH probes (Vaisala HMP50)	Mean T, RH	3, 10, 30	10
30	Thermocouples (Omega SSRTC-GG-K-36–36)	T	2, 3, . . . , 10, 12, 16, 20, 25, 30	10

know of no previous effort to incorporate spatially explicit plant area density information within a mesoscale meteorological model.

The procedure originated with two airborne lidar acquisitions: a 2004 Federal Emergency Management Agency (FEMA) acquisition [October 2004; leaf-on conditions; ~(80%–85%) of domain 5 covered] and a second acquisition that was collected the morning of the experiment (20 March 2011; leaf-off conditions; ~10% of domain 5 covered). A sequence of steps was executed to develop an A_p dataset representative of late winter foliage that was sufficiently large in areal coverage to be applied to domain 5. First, the methodology of Skowronski et al. (2011) was used to derive CHP at each lidar data pixel, for each acquisition. Second, linear regression models were developed to relate CHP to field-based estimates of A_p following the procedure described in Skowronski et al. (2011). Third, an existing forest cover map of New Jersey (Lathrop and Kaplan 2004) was utilized to assign forest cover type (e.g., pure pine, oak-dominated mixture) at data pixels where the two lidar acquisitions overlapped. Finally, linear regression models were developed for each forest cover type to relate leaf-on A_p from the FEMA acquisition to leaf-off A_p from the 20 March acquisition, and the regression models were applied to the entire FEMA dataset to yield a leaf-off A_p dataset for use with domain 5.

The A_p dataset is summarized in Fig. 3. In Fig. 3, horizontal plan view images of plant area index (PAI), defined as vertically integrated A_p, are displayed for domain 5 (Fig. 3a) and the area immediately surrounding the burn unit (Fig. 3b). Due to the fact that the northeast portion of the domain was outside the lidar field of view, the PAI in the northeasternmost 15%–20% of the domain is computed as the average of the PAI at all points in the domain where data exist. A large degree of heterogeneity is apparent across the domain, as well as in the vicinity of the burn unit, with the PAI inside the burn unit varying between 0 and about 1.6. Examining a vertical cross section of A_p oriented northwest–southeast through the 20-m tower location (Fig. 3c), we see a variety of different canopy structures, including surface-dominated vegetation, tall canopies with thin understory vegetation, and well-distributed canopies. Vertical profiles of A_p at grid points adjacent to the 20- and 30-m towers (Figs. 3d,e) complete the picture, further reinforcing the depiction of a horizontally and vertically heterogeneous forest canopy.

c. *Fire parameterization in ARPS-CANOPY*

Neither ARPS nor ARPS-CANOPY has a subgrid-scale fire parameterization or fire spread module. For the purpose of simulating the Butler Place fire, we utilize the following fire parameterization and configuration. As illustrated in Fig. 4a, a total of 125 grid cells are used to replicate the burn unit in ARPS-CANOPY, with the burn unit grid cells grouped into 10 northwest–southeast-oriented burn zones. Note that the model burn unit dimensions are consistent with those of the actual burn plot (1.9 km in the north–south direction; 0.9 km in the west–east direction, at widest point) (cf. Figs. 2 and 4a).

The first-order effect of the fire, heat, is represented in ARPS-CANOPY as an upward heat flux. Although debate exists in the research community as to whether the first-order effect of a fire should be represented as a surface heat flux or by a height-dependent heat flux profile, we opt to distribute the heat flux vertically based on both the recommendation of Sun et al. (2006b) and after analyzing the results of a series of ARPS-CANOPY simulations (not shown). Based on the sensitivity experiments, the vertical heat flux is specified up to 45 m above ground level (AGL) (2.5 times average canopy height), above which the heat flux is computed as in standard ARPS, via an eddy viscosity approach. The maximum heat flux is applied at the surface, followed by an exponential decay with an extinction coefficient of -0.024 up to 45 m AGL (based on sensitivity experiments).

Since ARPS-CANOPY does not have a subgrid fire spread module, representing a fire line that was no more than 10 m across at its widest point in a 100 m $\times$ 100 m grid-spacing simulation is a challenge (cf. scale of fire line in Fig. 4b to size of grid cells in Fig. 4a). For the purpose of this study, we assume that the peak 1-min mean vertical heat flux measured at the 20-m tower is reasonably representative of the heat flux from the fire before, during, and after the time when the fire line passes the 20-m tower location. We also assume that if the fire line were to pass through a hypothetical 100 m $\times$ 100 m area of the burn unit, at most 10% of that square would be burning at any given time. Based on the estimate of mean fire spread rate during the burn (1.5 m min^{-1}) and the peak 1-min mean heat flux observed at the 20-m tower (155 kW m^{-2}), a surface heat flux of 15.5 kW m^{-2} is applied steadily at all grid cells within burn zone 4, for a period of 98 min (1437–1615 EDT). In all other burn zones, an identical value of the surface heat flux is applied, although the timing and duration of the simulated fire is based on the timing of the fire-line passage at the other towers and simple interpolation (with extrapolation in the southwest and northeast corners of the burn unit, where data are lacking). The heat flux determined from the 20-m tower observations is utilized in all burn zones since the other towers were found to inadequately sample the meteorological

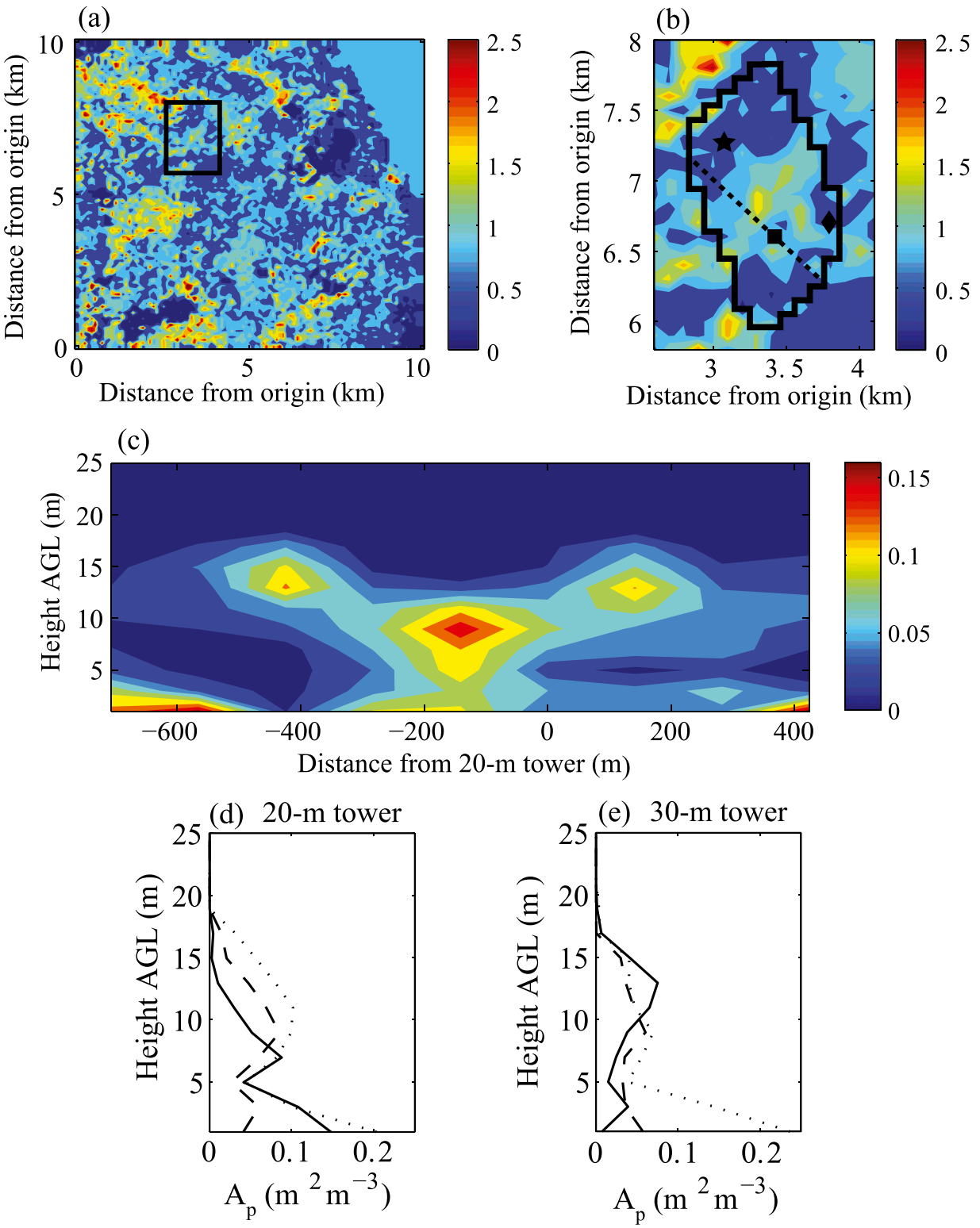

FIG. 3. Summary of plant area density dataset. Horizontal plan views of PAI for (a) all of domain 5 and (b) the area immediately surrounding the ARPS-CANOPY representation of the overlaid burn unit . The black rectangle in (a) denotes the outline of the area displayed in (b). (c) Vertical cross section of plant area density along axis denoted by the dashed line in (b). Vertical profiles of plant area density at three grid points nearest to the (d) 20- and (e) 30-m towers. The symbols in (b) indicate the locations of the 10- (star), 20- (square), and 30-m (diamond) towers.

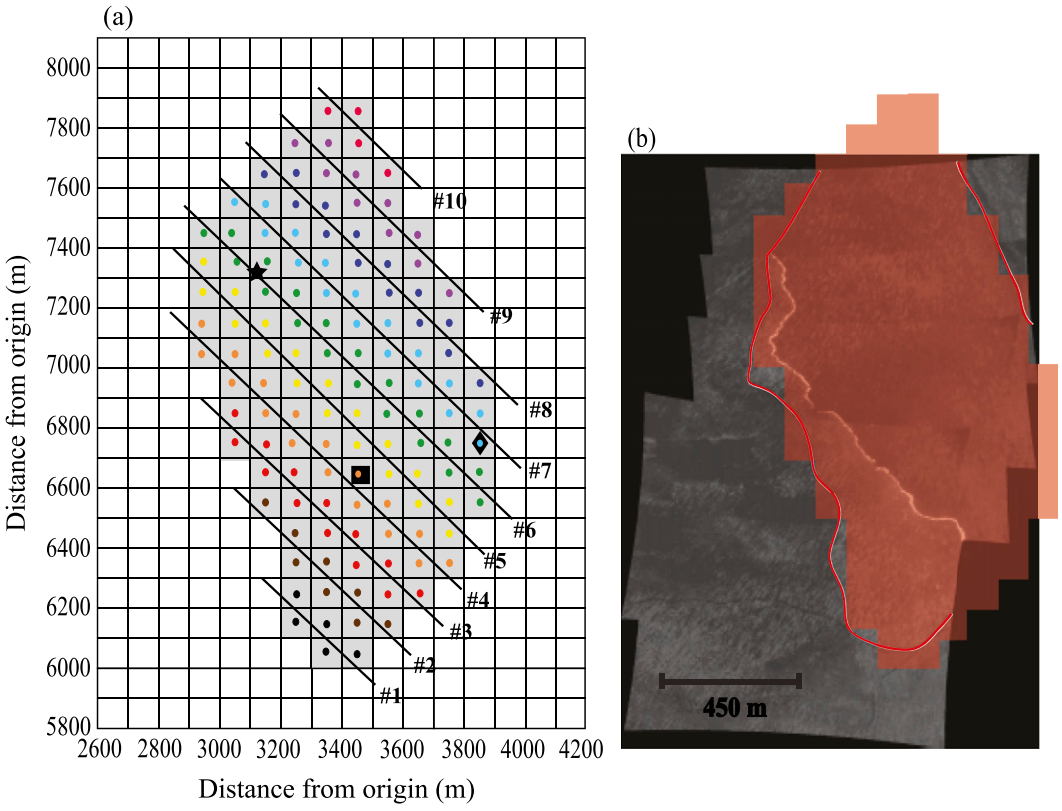

FIG. 4. Summary of (a) burn unit representation in ARPS-CANOPY with (b) longwave infrared (8–9.2 μm) image of the observed fire line at 1310 EDT (outline of actual burn perimeter is indicated by the red line and the footprint of the burn unit in ARPS-CANOPY is indicated by transparent red shading). The model representation of the burn unit consists of 125 cells on a 100 m × 100 m grid, organized into 10 groups or burn zones. In (a), each cell in the model burn unit is marked with a filled circle with each burn zone indicated by a different color. Consistent with the actual fire evolution, the simulated fire began at 0955 EDT in zone 1, and shifted gradually northeast through the burn unit until the end of the simulation at 2000 EDT. The symbols in (a) indicate the locations of the 10- (star), 20- (square), and 30-m (diamond) towers. See the text for a full description of the simulated fire configuration. In (b), the infrared image does not include the entire Butler Place plot as the north and southeast portions were outside of the field of view of the airborne instruments. (Infrared image courtesy of Rochester Institute of Technology.)

conditions near the fire line. Thus, only data from the 20-m tower are used for the micrometeorological analysis on 20 March.

4. Results and discussion

a. Synoptic-mesoscale overview

Before proceeding to the simulation of micrometeorology inside the burn unit, we examine the synoptic-mesoscale features on the day of and the day prior to the prescribed fire and compare the ARPS outermost-domain simulation (domain 1; Fig. 1a) with a reference dataset. NARR is chosen for this purpose as a matter of convenience, since it is used to define the initial and boundary conditions for the outermost-domain simulation. The NARR dataset is developed using first-guess fields supplied by the 32-km Eta Model (Mesinger et al. 1988; Janjić 1994) (rerun specifically for NARR), with observations assimilated as described in Mesinger et al. (2006); NARR is not intended here to represent "truth" but is used to corroborate the features identified in the ARPS simulation. With this caveat in mind, we present plots of sea level pressure, surface (i.e., lowest model level: z = 25 m AGL) temperatures, and wind vectors in Fig. 5, as well as 300-hPa geopotential heights, wind speeds, and wind vectors in Fig. 6, at 1400 EDT on both 19 and 20 March (1400 EDT is close to the time period of the micrometeorological analyses that follow).

During the 30 h prior to 1400 EDT 19 March, a cold front moved from a position over western New York and northwestern Pennsylvania at 0800 EDT 18 March to a position approximately 500 km east of the New Jersey coastline at 1400 EDT 19 March (not shown). At 1400 EDT 19 March, NARR surface fields (Fig. 5a)

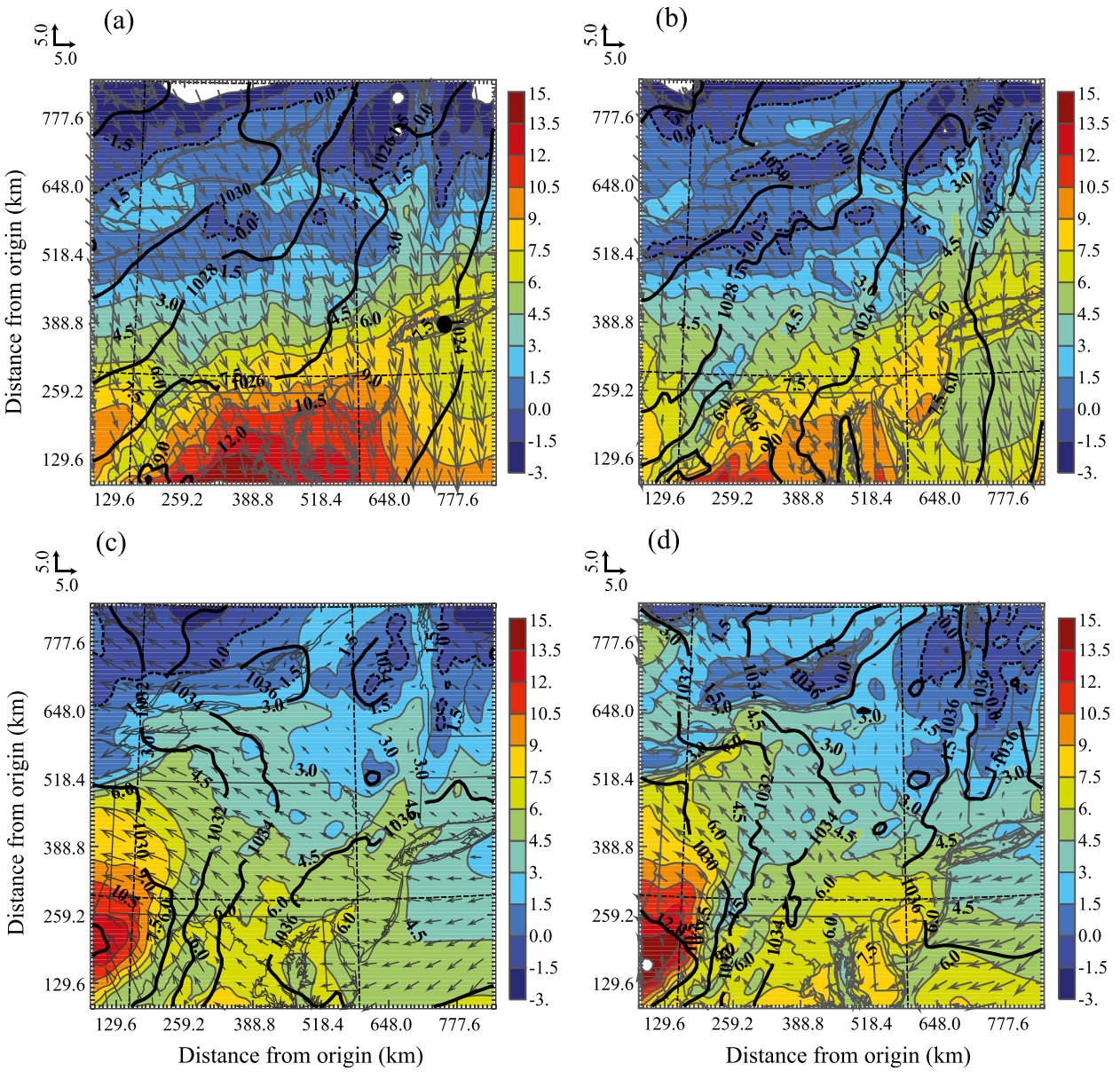

FIG. 5. Surface temperature (color shaded; °C), wind vectors (m s^{-1}), and sea level pressure (contoured every 2 hPa) at 1400 EDT (a),(b) 19 and (c),(d) 20 Mar 2011 from (left) NARR and (right) the ARPS domain-1 simulation with the boundary zone omitted. Note that the NARR fields have been interpolated to the ARPS model grid for comparison and that the surface is defined in ARPS as the lowest model level (in this case, 25 m AGL). The vector scale is located above figure panels to the left. Black circle in (a) indicates the location of OKX; see upper-air sounding assessment in Fig. 7.

depict a regime of cold-air advection over the northeast United States, with high pressure centered just south of James Bay, Canada (not shown). A thermal ridge is positioned along the mid-Atlantic coastal plain, the result of downsloping northwest flow in the lee of the Appalachian Mountains (see terrain in Fig. 1a). Meanwhile at 300 hPa (Fig. 6a), west-to-northwest flow is present, with a trough axis and associated jet maximum located east of the analysis region, with the 55 m s^{-1} isotach extending as far west as northeast Pennsylvania.

At 1400 EDT 20 March (Fig. 5c), a broad area of high pressure is centered east of New Jersey, with east-southeasterly winds indicated over central New Jersey. In contrast to the 19 March surface analysis, the warmest temperatures are located west of the Appalachian Mountains, with temperatures over central New Jersey 2°–4°C cooler than the day before

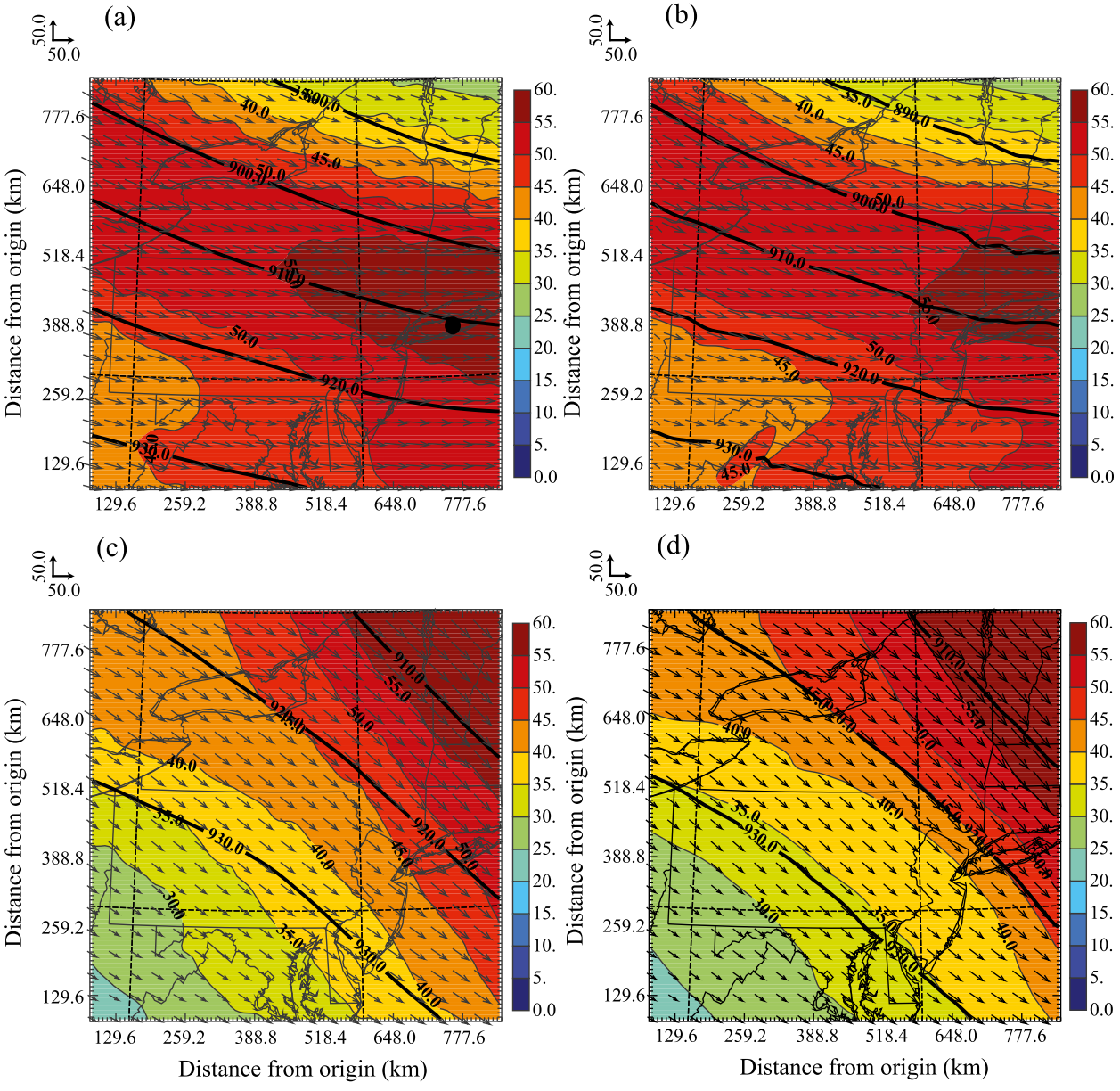

FIG. 6. As in Fig. 5, but for the 300-hPa wind speed (color shaded; m s^{-1}), geopotential heights (contoured every 10 dam), and wind vectors (m s^{-1}).

(cf. Figs. 5a and 5c). Furthermore, surface winds over central New Jersey are considerably weaker on 20 March (3 versus 6 m s^{-1}). At 300 hPa (Fig. 6c), the trough axis has moved to the east and the upper-level jet is now present mainly over northern New England, with northwesterly winds over the experiment site.

Upon comparing the left and right panels of Figs. 5 and 6, a number of differences between the NARR and ARPS fields become apparent. Beginning with 19 March, we see that surface temperatures across approximately the southern third of the domain are 2°–3°C colder in ARPS than NARR, the result of a too-early passage of the aforementioned cold front in ARPS and, consequently, a longer period of cold advection. The early passage of the cold front is consistent with the farther east placement of the 300-hPa jet maximum in ARPS compared to NARR (cf. Figs. 5a,b and 6a,b). Despite the surface temperature disparity, ARPS does capture the thermal ridge on 19 March, and temperature differences over central New Jersey are less than 1.5°C. However, surface wind speeds are consistently weaker over land in ARPS, compared to NARR. Comparison to observed

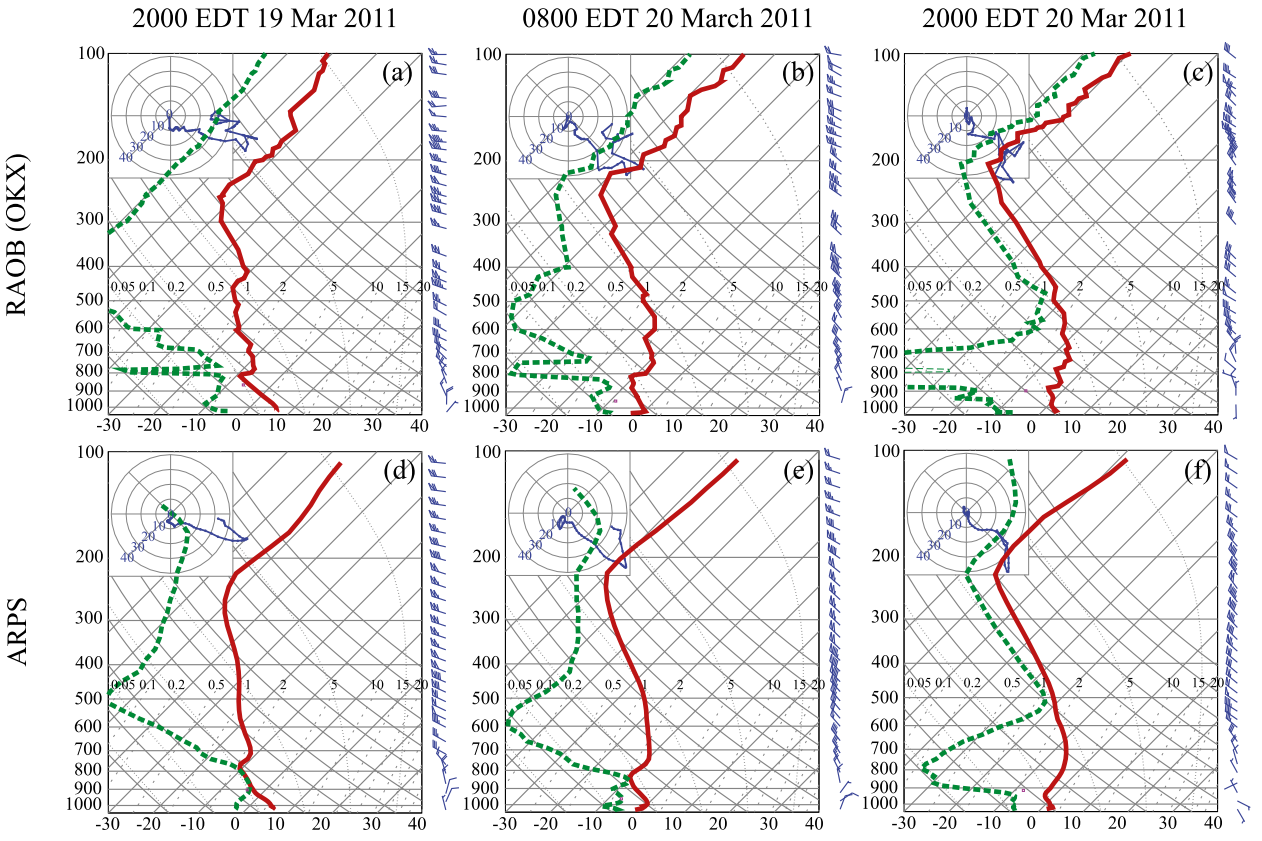

FIG. 7. Comparison of (a)–(c) rawinsonde (raob) sounding at OKX, and (d)–(f) ARPS model sounding at the same location. In all panels, the red line is temperature and the green line is dewpoint; the blue curve in the top-left corner of each panel indicates the hodograph trace. Location of OKX is indicated by a black circle in Figs. 5 and 6.

10-m wind speeds (not shown) suggests that the ARPS 25-m wind speeds are indeed too weak, although as will be discussed in the micrometeorology analysis in section 4b, any wind errors in the coarse-grid simulations do not extend to the innermost-domain simulation. Finally, surface temperatures on 20 March over southern New Jersey and the Delmarva region are 2°–3°C warmer in ARPS than NARR; a review of surface observations (not shown) suggests that ARPS more closely approximates the observed temperature on this day.

To assess the vertical structure of the atmosphere in ARPS, we present vertical soundings of temperature and dewpoint on a skew T–log$p$ diagram, along with hodographs and wind vectors, as observed at Brookhaven, New York (OKX; see black circle in Fig. 5a), and as simulated by ARPS, at 2000 EDT 19 March, 0800 EDT 20 March, and 2000 EDT 20 March (Fig. 7). As shown in Fig. 7, the observed and model soundings generally agree, with both depicting a subsidence inversion gradually descending from near 800 hPa at 2000 EDT 19 March to near 900 hPa at 2000 EDT 20 March. Examining the two evening soundings (2000 EDT 19 and 20 March; Figs. 7a,d and 7c,f), it is clear from both ARPS and the OKX sounding that a considerably shallower boundary layer was present on 20 March than on 19 March. The shape and orientation of the hodographs, as well as the wind vector profiles, indicate a shift in mid- and upper-level flow from westerly to northwesterly during the 24-h period (in agreement with Fig. 6); ARPS and the OKX sounding show agreement with regard to the wind. The only consistent model bias seen in the ARPS soundings is a tendency for the simulation to be too moist below the subsidence inversion, particularly at 2000 EDT 19 March (cf. Figs. 7a and 7d).

b. *Micrometeorology evaluation*

1) 19 MARCH: PREBURN DAY

We begin the micrometeorological analysis of the Butler Place burn experiment with an evaluation of the 19 March preburn simulation (initialized at 0800 EDT 19 March). Figures 8 and 9 depict vertical profiles of mean TKE, wind speed and direction, and temperature, at the 20- and 30-m towers, respectively, from an ARPS-CANOPY simulation

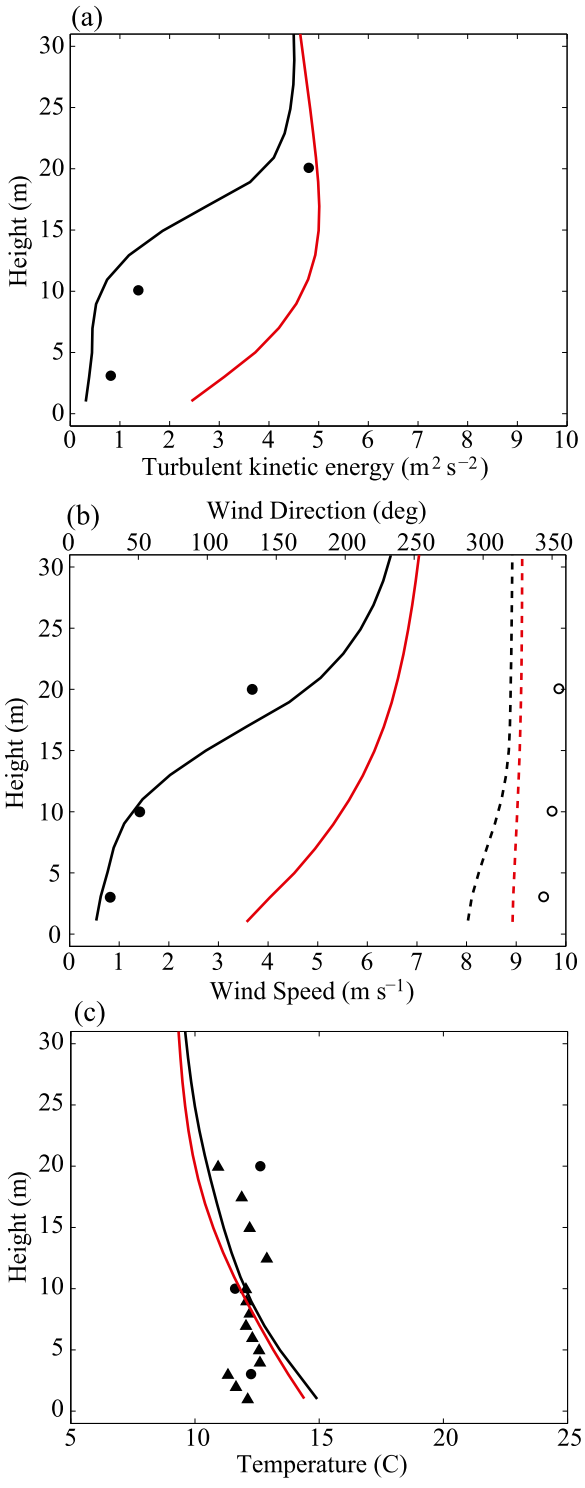

FIG. 8. Vertical profiles of (a) TKE, (b) wind speed and direction, and (c) temperature averaged in time from 1430 to 1730 EDT 19 Mar 2011, at the 20-m tower. ARPS-CANOPY-simulated fields are averaged around three grid points in the vicinity of the 20-m tower. Symbols represent tower observations: sonic anemometer measurements (circles) and thermocouple measurements (triangles). In (b), filled circles/solid lines indicate wind speed, and open circles/dashed lines are wind direction. Simulations with zero (nonzero) plant area density are indicated with red (black) lines.

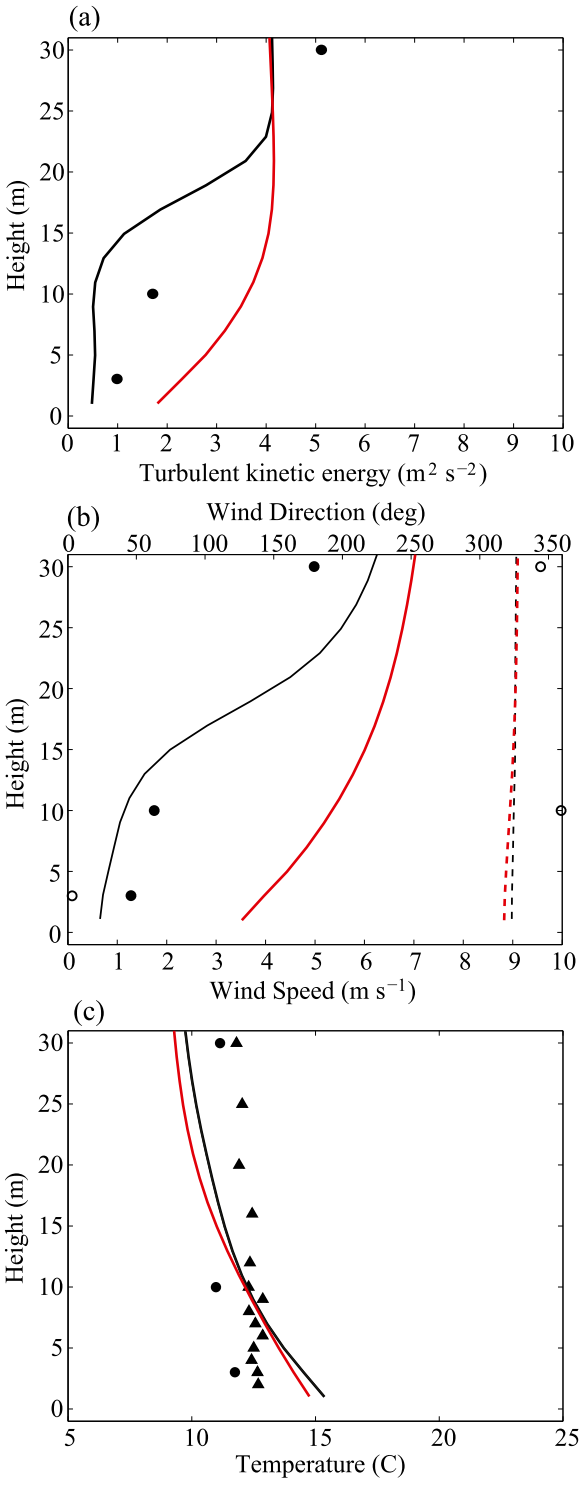

FIG. 9. As in Fig. 8, but for the 30-m tower.

utilizing the lidar-derived A_p profiles described in section 3b (black lines) and a simulation where A_p is set to zero everywhere in the model domain (red lines). To compute grid-resolved TKE, the three instantaneous wind

components are individually averaged over a 1-h time period; the perturbation wind components (u', v', w') are computed by subtracting the 1-h mean from the instantaneous value, and instantaneous turbulent kinetic energy is subsequently computed as $\frac{1}{2}(u'^2 + v'^2 + w'^2)$. Although 30-min averages are commonplace in the computation of turbulence from point observations, a 1-h-averaging period has been identified by Sun et al. (2006c) as being critical to capturing all scales of turbulence at forested sites. Following the computation of resolved TKE, all variables are averaged from 1430 to 1730 EDT, and in the case of the simulated variables are also averaged over three grid points in the vicinity of each tower. Note that the simulated TKE displayed in each of the figures is the total TKE, the sum of the resolved component and the subgrid-scale component computed by ARPS (via a prognostic equation). The reader is reminded that the 20-m tower is contained almost entirely within the canopy (Fig. 3d) and the lowest $\frac{2}{3}$ of the 30-m tower are located inside the canopy (Fig. 3e).

We start with an assessment of the ARPS-CANOPY simulation conducted using the lidar-derived A_p profiles (black lines). Data at the 20-m tower show that the shape of the mean TKE profile is captured by the ARPS-CANOPY simulation, although the model underestimates TKE by 0.5–1 $m^2 s^{-2}$ (Fig. 8a). For mean wind speed and direction (Fig. 8b), the shapes of the ARPS-CANOPY profiles are similar to the shapes of the observed profiles, with some overestimation in wind speed at the 20-m level, and a bias in wind direction of approximately 30° throughout the profile (the bias is larger at the 3-m level; however, the wind is less than 1 $m s^{-1}$ there). Finally, the simulated and observed mean temperature profiles roughly correspond (Fig. 8c), although simulated temperatures below (above) 10 m AGL are too warm (cool). Temperature inversions appear in the thermocouple observations near 3 m AGL and above 10 m AGL; the inability of ARPS-CANOPY to replicate the inversions may result from inadequacies in the lidar-derived plant area density data (Fig. 3), limitations of the canopy heat source parameterization, and mixing of finescale gradients by the subgrid turbulence parameterization.

The assessment of the mean profiles at the 30-m tower (Fig. 9) is similar to the assessment of the 20-m tower profiles, although the errors in mean wind speed and TKE are somewhat larger and the errors in mean wind direction are somewhat smaller at the 30-m tower (cf. Figs. 8a,b and Figs. 9a,b). Slightly larger model errors in mean temperature are apparent at the 30-m tower, although the aforementioned tendency for temperatures below (above) 10 m AGL to be too warm (cool) is also apparent there. Note that in contrast to the thermocouple measurements at the 20-m tower, the temperature observations at the 30-m tower indicate an isothermal near-surface atmosphere. The model errors in TKE, wind, and temperature at the two towers are within the margin of error noted in Kiefer et al. (2013) regarding ARPS-CANOPY simulations of the atmosphere observed in and above a walnut orchard during the CHATS experiment. No consistent model biases have to date been identified with ARPS-CANOPY, although a tendency to produce temperature profiles that are too weakly mixed was noted in Kiefer et al. (2013), as well as in this study (e.g., Figs. 8c and 9c).

Comparison of the model simulation with observed A_p (black lines) to the corresponding simulation with A_p set to zero (red lines) illustrates the importance of the canopy parameterization to the simulation of mean wind and TKE, particularly inside the canopy. Without a forest canopy in the model, the mean TKE at and below 18 m AGL is overestimated by 1–3 $m^2 s^{-2}$ (Figs. 8a and 9a) and the mean wind speed is 2–4 $m s^{-2}$ too strong (Figs. 8b and 9b). Wind direction (Figs. 8b and 9b) and temperature (Figs. 8c and 9c) exhibit limited sensitivity to the canopy parameterization, likely related to the sparse nature of the forest canopy near the two towers (Fig. 3). Additional experiments with ARPS-CANOPY using idealized A_p profiles have shown a stronger sensitivity of mean wind direction and temperature to the canopy parameterization when dense canopies (PAI = 5+) are compared with no or sparse vegetation (not shown).

2) 20 MARCH: BURN DAY

We now proceed to an analysis of the mean and turbulent properties of the atmosphere above the parameterized fire on 20 March, as simulated by ARPS-CANOPY (simulation initialized at 0800 EDT 20 March). The methodology utilized to generate the vertical profiles differs from the 19 March analysis as follows. First, all fields on 20 March are averaged from 1510 to 1610 EDT, in contrast to the 3-h average used on 19 March (although perturbations are derived from 1-h mean fields, as outlined in the previous section). On 19 March, an assumption of quasi-stationarity during the afternoon is made, based on an evaluation of the tower observations. On 20 March, the period from 1510 to 1610 EDT approximately corresponds to the period of time (1514–1607 EDT) during which observed vertical turbulent heat fluxes ($w'T'$) on the 20-m tower were elevated above the background values (Heilman et al. 2013). Second, because the ARPS-CANOPY fire configuration involves distinct burn zones with identical fire timings at all grid points in the same zone (section 3c; Fig. 4), the time-averaged model fields are also averaged across all grid points in zone 4 (the zone corresponding to the 20-m tower). Finally, to account for the variation between

model grid points in the same burn zone, mean fields ±1 standard deviation (perturbations from the burn zone mean) are also included. Note that wind direction is omitted from the analysis on 20 March; the differences in fire characteristics between the real fire and the parameterized fire (e.g., intensity, fireline width) and the averaging of model results along the model fire line make a comparison of mean wind direction inappropriate.

In Fig. 10, we compare the ARPS-CANOPY simulation on 20 March with the corresponding observations at the 20-m tower. Examining mean TKE first (Fig. 10a), we see that as on the preburn day (Fig. 8a), the shape of the TKE profile is similar to the shape of the observed profile, but there are errors in magnitude. ARPS underestimates the mean TKE at 20 m AGL, while overestimating the mean TKE at 3 and 10 m AGL; the observation points are, however, within 1 standard deviation of the ARPS mean at 10 and 20 m AGL. Regarding mean wind speed (Fig. 10b), we see that the ARPS mean profile nearly matches the observed wind speed profile, with the pattern of over/underestimation similar to the TKE profile. Of great importance is the comparison of the mean profile in the simulations with and without a fire: removal of the fire yields considerably smaller mean TKE and wind speed and, subsequently, greater model error. For reference, note that the mean TKE observed at 20 m AGL prior to the approach of the fire line was 2.72 $m^2 s^{-2}$ (1410–1510 EDT mean; not shown), in close agreement with the ARPS mean TKE in the no-fire simulation (1510–1610 EDT mean; Fig. 10a).

Interestingly, the shapes of the mean TKE and wind speed profiles above the simulated fire appear to be determined primarily by the canopy structure and, to a lesser degree, by the fire. This is consistent with the findings of the 19 March no-canopy sensitivity experiments discussed earlier, wherein the shape of the profiles was shown to be in poor agreement with observations when the canopy was omitted. The 20 March profile shapes strongly resemble those simulated on 19 March (cf. Figs. 10a,b with black lines in Figs. 8a,b and 9a,b). Note the correspondence between the layer of strong vertical gradients in mean wind and TKE (12–20 m AGL in Figs. 10a,b) and the layer of strong plant area density gradients in the upper canopy (Fig. 3d). The maximum in mean TKE is displaced above the canopy top, as is typical of plant canopies (Raupach and Thom 1981). Furthermore, the secondary maximum in mean TKE near 5 m AGL corresponds to a relatively thin area of the canopy near that same height. However, it is worth noting that the secondary maximum in TKE becomes much less pronounced when the fire is omitted, with the TKE shape inside the canopy closely resembling the shape of the

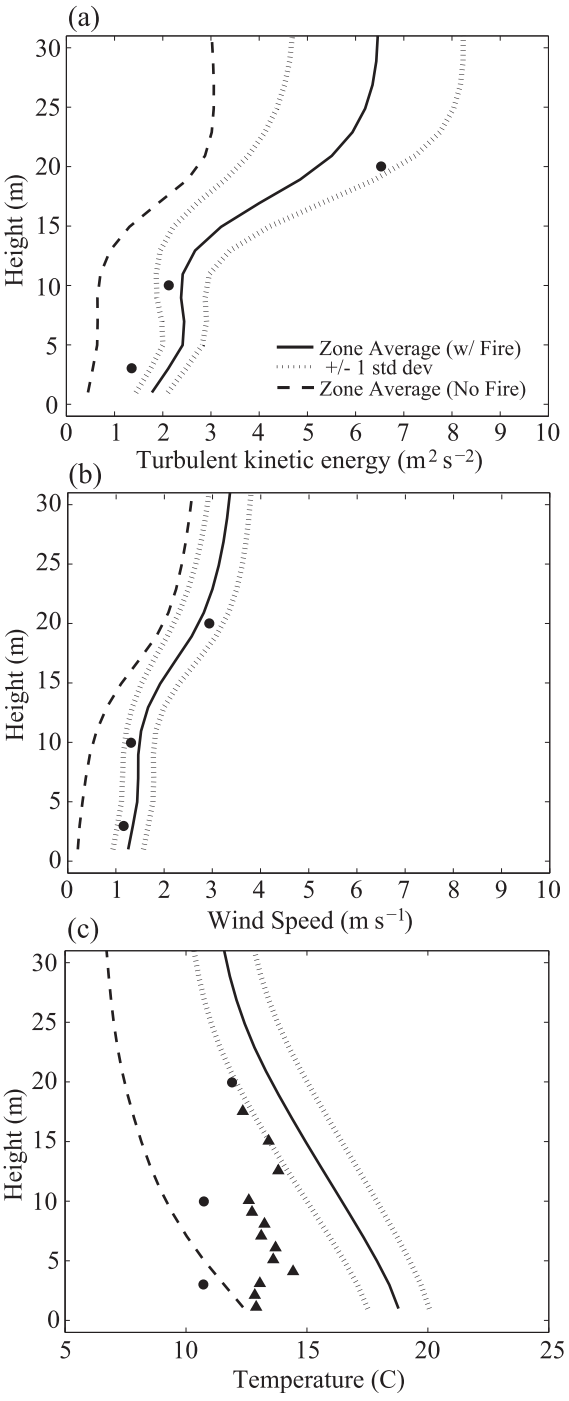

FIG. 10. Vertical profiles of (a) TKE, (b) wind speed, and (c) temperature, averaged from 1510 to 1610 EDT 20 Mar 2011. ARPS-CANOPY-simulated fields are averaged around all grid points in burn zone 4 (see Fig. 4a); solid lines indicate the mean, and dotted lines indicate the mean ±1 standard deviation (perturbations computed with respect to burn zone mean). Long dashed line indicates mean from simulation without a fire. Symbols represent tower observations: sonic anemometer measurements (circles) and thermocouple measurements (triangles).

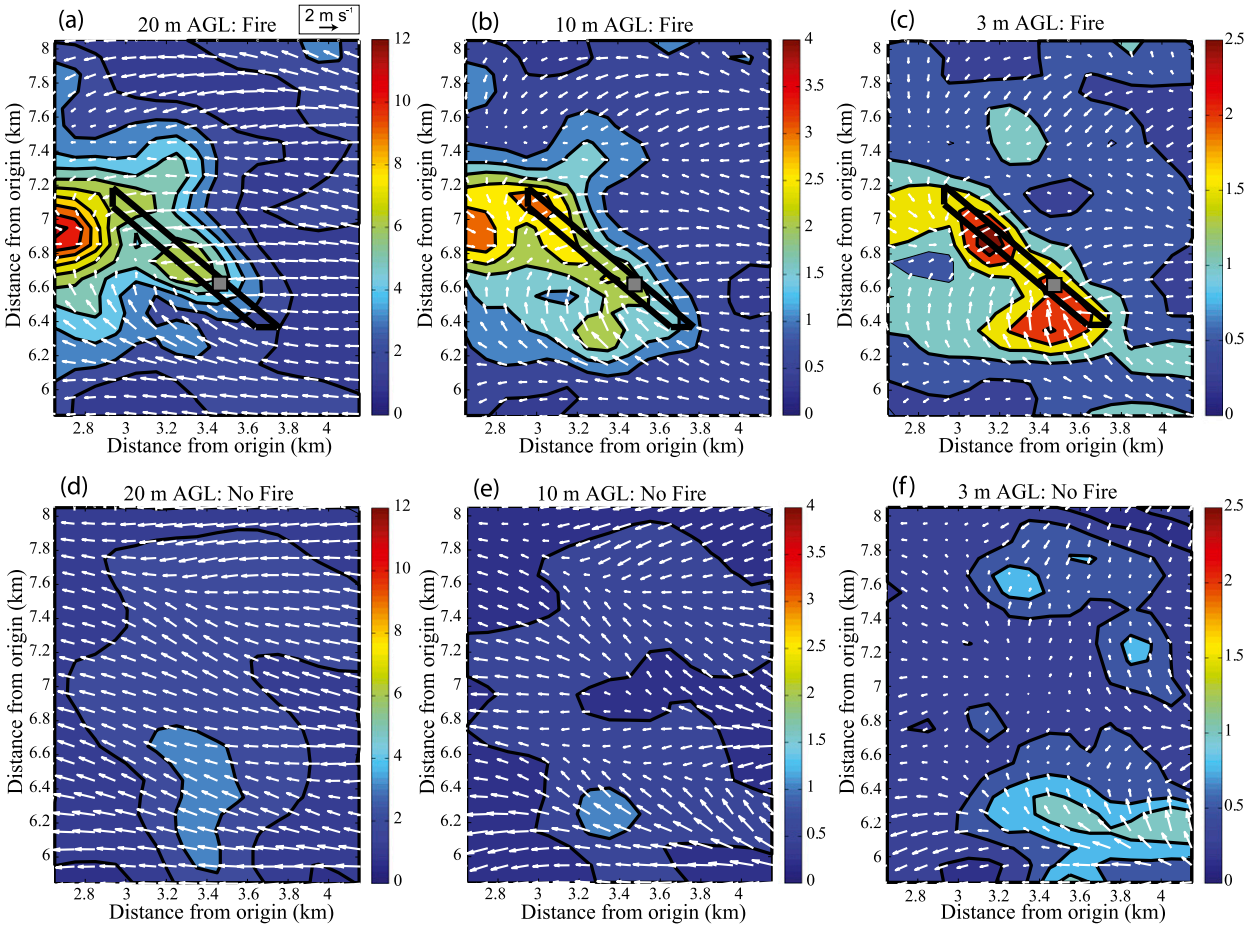

FIG. 11. TKE (color shaded and contours) at (a),(d) 20, (b),(e) 10, and (c),(f) 3 m AGL, averaged from 1510 to 1610 EDT 20 Mar 2011 from ARPS-CANOPY simulations (top) with fire and (bottom) without fire. Horizontal wind vectors are overlaid along with the perimeter of burn zone 4 (black quadrilateral) and the position of the 20-m tower (gray square). Contour interval in (a) and (d) is 1 $m^2 s^{-2}$, and in all other panels the interval is 0.5 $m^2 s^{-2}$; note the difference in the color bar limits between the panels.

mean TKE profiles on 19 March (cf. dashed line in Fig. 10a to Figs. 8a and 9a).

Regarding the simulation of mean temperature above the fire line (Fig. 10c), we find that similar to the 19 March assessment, the model generally reproduces the observed lapse rate, while the magnitudes differ. Although errors approach or even exceed 6°C near the surface, several factors must be considered when evaluating the 20 March ARPS-CANOPY simulation. First, the 1-h average of the tower data includes the period of time before and after the passage of the relatively intense, but narrow fire line, while the use of 100-m grid spacing necessitates the application of the relatively weak, but longer-duration heating in the model. Second, since the tower was surrounded by an area with limited fuels, the temperature sensors closer to the surface did not sense the full heat from the fire. Third, regarding the application of ARPS-CANOPY to the problem of smoke dispersion, the absolute magnitude of the temperature is less important than the lapse rate. Implementation of the simple fire parameterization in ARPS-CANOPY yields a simulation of mean and turbulent flow that agrees with the tower observations during the period of time the tower experienced perturbed atmospheric conditions due to the proximity of the fire.

We now examine horizontal cross sections of simulated mean TKE and wind in and around the model burn unit (Fig. 11). Analysis is limited to three levels: 3, 10, and 20 m AGL (top panels in Fig. 11). Corresponding plots from the no-fire simulation are also included in Fig. 11 for comparison (bottom panels in Fig. 11). The horizontal cross sections from the simulation with fire (Figs. 11a–c) depict a broad area of enhanced mean TKE in the fire simulation that is not present when the fire is omitted (Figs. 11d–f). Interestingly, this "fire induced" TKE is found not only along the axis of burn

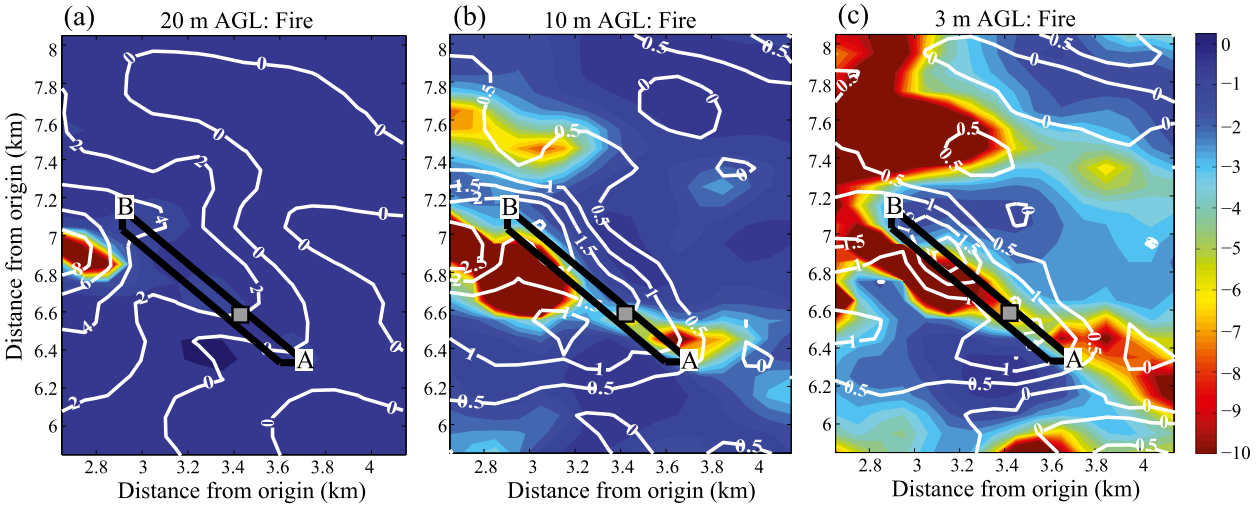

FIG. 12. Gradient Ri (shaded; interval is 0.5) at (a) 20, (b) 10, and (c) 3 m AGL averaged from 1510 to 1610 EDT 20 Mar 2011 from ARPS-CANOPY simulations with the parameterized fire. Overlaid is the difference field of TKE (fire − no fire); contour interval is 2 $m^2 s^{-2}$ for (a) and 0.5 $m^2 s^{-2}$ for (b) and (c). As in Figs. 11a–c, the perimeter of burn zone 4 (black quadrilateral) and the position of the 20-m tower (gray square) are indicated. Labels A and B correspond to *y*-axis labels in Fig. 13, below.

zone 4 (denoted by the black quadrilateral) but well away from the fire itself. In fact, the largest TKE value at 20 m AGL is located several hundred meters west of the fire, at the western edge of the analysis area. The impact of the fire on the horizontal wind field is manifested as a broad zone of convergent winds in an otherwise easterly to southeasterly flow. While alternating bands of confluent and diffluent winds indicative of convective structures in the planetary boundary layer can be seen in the no-fire simulation (Figs. 11d–f), convergent wind vectors in the vicinity of the fire indicate the influence of the surface heat source.

Figure 11 shows that the fire simulation produced TKE perturbations well away from the location of the fire line. To determine the generation mechanism for this perturbation, we evaluate gradient Richardson number (Ri), a metric that compares the relative roles of buoyant production (or destruction) and shear production in the generation of TKE. The Ri is defined as

$$\frac{\dfrac{g}{\overline{\theta}}\dfrac{\partial\overline{\theta}}{\partial z}}{\left(\dfrac{\partial\overline{u}}{\partial z}\right)^2+\left(\dfrac{\partial\overline{v}}{\partial z}\right)^2}, \tag{1}$$

where $\overline{\theta}$ is mean potential temperature, and $\overline{u}$ and $\overline{v}$ are the mean u and v wind components. Positive values of Ri imply that buoyancy suppresses turbulence generated by vertical wind shear, while negative values of Ri imply buoyancy contributes to turbulence production. Generally, Ri less than about −0.03 indicates buoyant production is the dominant source of TKE, while $-0.03 < \mathrm{Ri} < 0$ suggests that both buoyancy and shear production contribute to turbulence generation (Seinfeld 1975).

Plots of Ri at 3, 10, and 20 m AGL from the fire simulation are presented, with the TKE difference (fire − no fire) overlaid, in Fig. 12. The Ri is less than −0.5 almost everywhere, with the exception of a small area in the south-central part of the analysis region where Ri at 20 m AGL is weakly positive. Outside of that small area, the analysis indicates that buoyancy is the dominant source of TKE. However, a wide range in negative Ri values is apparent at all levels, with Ri varying from less than −10 (dark red shading) to approximately −0.5 (dark blue shading). At all three levels, a stripe of strongly negative Ri is seen to extend from near $(x, y) = (2.7, 7.0)$ km to near $(x, y) = (3.8, 6.4)$ km [i.e., along and to the southwest (downstream) of the axis of burn zone 4]. However, the axis of largest TKE increase, relative to the no-fire simulation, is consistently along and to the northeast of the stripe of strongly negative Ri (i.e., closely aligned with burn zone 4). Farther away from that axis, buoyancy is still dominant, but shear plays an important secondary role. An exception to this is the area of fire-enhanced TKE several hundred meters west of the fire line [$(x, y) = (2.7, 6.9)$] at 20 m AGL (Fig. 12a). This area of TKE likely results from advection of TKE generated above the fire line by the ambient easterly flow and advection of the heated air (and displacement of buoyancy production) west of the fire line (note the area of $\mathrm{Ri} < -10$ collocated with the TKE difference maximum).

We have established that ARPS-CANOPY is capable of reproducing the shape of the 1-h mean TKE profile, with some errors in magnitude, and that the introduction of the model fire parameterization results in a broad area of enhanced TKE (relative to a no-fire simulation) that is generated by buoyancy and, to a lesser extent, vertical wind shear. Before concluding the ARPS-CANOPY analysis, we wish to address the evolution of 1-min mean TKE along burn zone 4 and compare the magnitude of the simulated TKE to tower observations (Fig. 13). Our goal here is to gauge the ability of the model to reproduce the range of 1-min mean TKE observed at the tower location between 1510 and 1610 EDT. It should be noted that the same 1-h averaging procedure outlined in the previous section is utilized; the 1-min mean refers to the averaging of the TKE time series. In Figs. 13a–c, it is apparent that simulated 1-min mean TKE is not only highly variable along the fire-line axis, but is also unsteady in time, despite the application of a steady heat source. The larger TKE values are confined to roughly the northwestern half of the burn zone, although time periods exist when TKE is suppressed along the entire length of the zone (e.g., around 1524 EDT). Finally, regarding the magnitude of simulated TKE at 20, 10, and 3 m AGL, note that the peak 1-min simulated TKE values (20 m, 20.51 $m^2 s^{-2}$; 10 m, 6.45 $m^2 s^{-2}$; 3 m, 7.03 $m^2 s^{-2}$) compare favorably to the peak observed values (20 m, 20.49 $m^2 s^{-2}$; 10 m, 8.21 $m^2 s^{-2}$; 3 m, 6.80 $m^2 s^{-2}$) at the tower location (Fig. 13d). Note that since the heat source observed at the 20-m tower was transient, and the heat flux is applied steadily in each model grid cell for a 98-min period, we are not comparing the timing of peak TKE between the observations and the model, only their overall magnitudes.

5. Summary and conclusions

We have described herein the application of ARPS-CANOPY to the simulation of meteorological conditions in and around a low-intensity fire in the New Jersey Pine Barrens. In ARPS-CANOPY, the drag and thermodynamic processes inside the canopy are parameterized as a function of plant area density; a three-dimensional lidar-derived plant area density dataset was utilized in this study to define the canopy in detail. Furthermore, the finescale combustion process was reduced to a heat source on the resolved model grid, and the progression of the fire through the roughly 1-km^2 burn unit was represented as a gradual progression from southwest to northeast. An assessment of the outermost grid simulation was conducted first, followed by comparisons of mean and turbulent flow simulated with

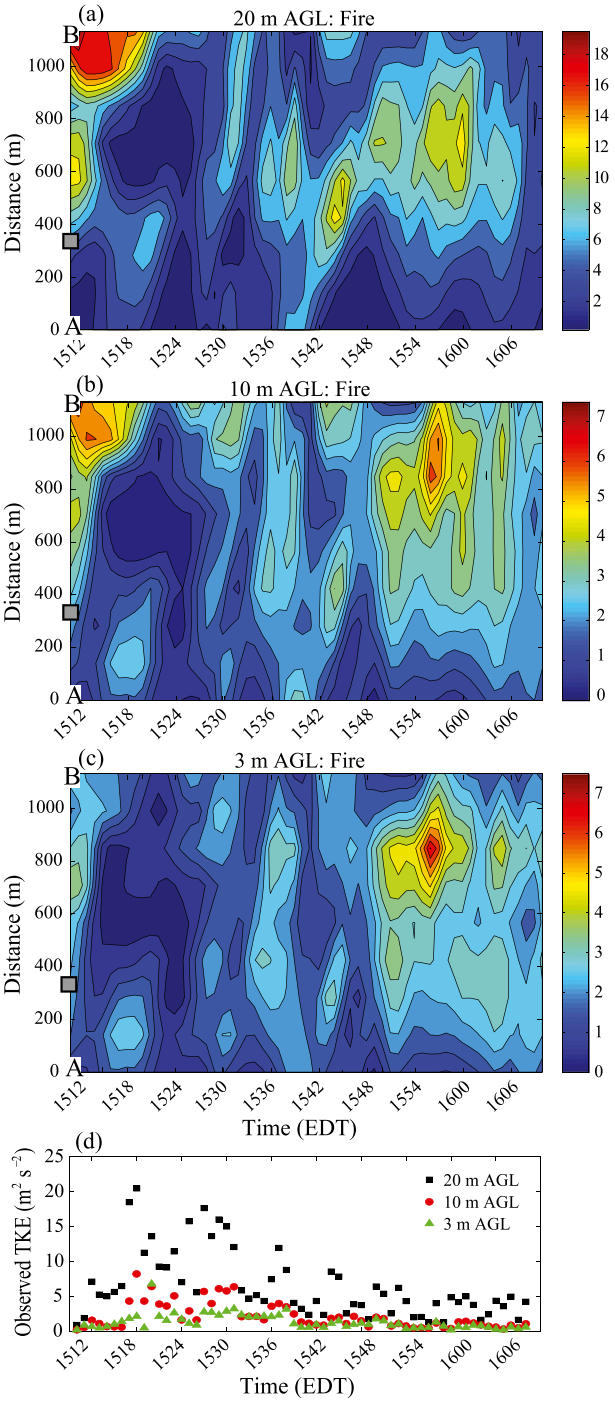

FIG. 13. Hovmöller diagram of simulated 1-min mean TKE at (a) 20, (b) 10, and (c) 3 m AGL from 1510 to 1610 EDT 20 Mar 2011. (d) Observed 1-min mean TKE over the same period and at the same levels. In (a)–(c), the vertical axis is the distance along burn zone 4 from the southeast (label A) to northwest (label B), where $y = 0$ is the southeasternmost grid point and the horizontal axis is time; gray square along the vertical axis denotes the location of the 20-m tower. See Fig. 12 for locations of labels A and B along the burn zone. Contour interval in (a) is 1.5 $m^2 s^{-2}$ and in other panels is 0.5 $m^2 s^{-2}$; note the difference in the color bar limits between panels.

ARPS-CANOPY with flux-tower observations on the day prior to the burn (19 March), as well as on the burn day itself (20 March).

Despite some discrepancies between the model and observations, the ARPS model was shown to be capable of simulating the atmosphere at the synoptic and mesoscales, as well as the salient aspects of the planetary boundary layer. Regarding the micrometeorological analysis on 19 March, ARPS-CANOPY profiles of mean TKE, wind speed–direction, and temperature were found to reasonably reproduce the characteristics of the tower observations. The shapes of the mean simulated TKE and wind speed–direction profiles were supported by the tower measurements, as were the lapse rates in and above the canopy. Most importantly, implementation of the simple fire parameterization in ARPS-CANOPY was shown to yield profiles of mean and turbulent variables that were also apparent in the tower observations on 20 March, during the period of time the tower experienced perturbed atmospheric conditions associated with the fire. Such findings are encouraging for smoke prediction efforts, since the transport of smoke from low-intensity fires can be sensitive to the near-surface meteorological conditions and, in particular, turbulent flows. Turbulent circulations in and above forest vegetation layers can have a strong impact on the dispersion of smoke in the lower boundary layer. Following the model evaluation, an analysis of simulated mean TKE cross sections within the burn unit and surrounding area was conducted. Considerable variability in mean TKE both spatially and temporally was noted, and it was concluded that buoyancy was the dominant turbulence generation mechanism throughout the model domain, with shear playing a secondary role away from the immediate fire line. Note that since the burn was conducted during weak ambient wind conditions (5–8 m s^{-1} or less), findings regarding turbulence production may not extend to cases with stronger background flow.

Although agreement with observations was noted on both days, model error was present to some degree for each variable examined. On 19 March, the mean TKE at both towers was underestimated, the mean wind speeds were too weak (too strong) below (above) canopy top, and a wind direction bias of 25°–30° was apparent throughout the profiles. The tendency of ARPS-CANOPY to produce temperatures that are too warm near the surface and too cool above the canopy was also noted. Similar magnitudes and signs of model error were also found on 20 March, although temperatures were uniformly overestimated above the fire line. It is important to note, however, that observed mean TKE, wind speed, and temperature were generally within one standard deviation (deviation from burn zone mean) of the ARPS-CANOPY mean. This implies that although mean TKE, for example, may have been underestimated above the canopy in the immediate vicinity of the 20-m tower, larger values were simulated elsewhere along the fire line.

Regardless of limitations, ARPS-CANOPY has been shown in this study to reproduce many of the salient characteristics of flow within a canopy, both with and without a low-intensity fire; and that could be important for smoke dispersion predictions. At this time, ARPS-CANOPY is being applied to a second prescribed fire case in the Pine Barrens (5–6 March 2012). Evaluation efforts with the Pacific Northwest National Laboratory Integrated Lagrangian Transport (PILT) model [a recently revised version of the FLEXPART model (Stohl et al. 2005; Fast and Easter 2006)] are also ongoing, as the meteorological fields from the 2011 and 2012 cases are provided as input into the smoke dispersion model. Future work with PILT will include simulating smoke transport and dispersion with standard ARPS and ARPS-CANOPY models to examine the relative roles of model resolution and canopy parameterization in the simulation of smoke behavior observed during prescribed burn events. Other future efforts include developing an operational version of ARPS–ARPS-CANOPY that will allow users to input information about a planned burn and receive smoke and meteorological predictions in real time. The availability of a smoke prediction product designed specifically for application to low-intensity burns is expected to be of value to land management personnel. Developing useful smoke prediction tools and making them accessible to land managers for decision-making purposes is the principal motivation behind such work.

Acknowledgments. Support for this research was provided by the U.S. Joint Fire Science Program (Project 09-1-04-1) and the USDA Forest Service (Research Joint Venture Agreement 09-JV-11242306-089). Special thanks are given to the N. J. Forest Fire Service for conducting the burn and Bob Kremens for use of the infrared imagery of the fireline. We also thank Alan Srock, Jovanka Nicolic, and three anonymous reviewers for providing helpful comments and suggestions to improve the manuscript.

REFERENCES

Chou, M.-D., 1990: Parameterization for the absorption of solar radiation by O_2 and CO_2 with application to climate studies. *J. Climate,* **3,** 209–217.

——, 1992: A solar radiation model for climate studies. *J. Atmos. Sci.,* **49,** 762–772.

——, and M. J. Suarez, 1994: An efficient thermal infrared radiation parameterization for use in general circulation models. NASA Tech. Memo. 104606, 85 pp. [Available from NASA

Center for Aerospace Information, 800 Elkridge Landing Rd., Linthicum Heights, MD 21090-2934.]

Colette, A. G., F. Katopodes Chow, and R. L. Street, 2003: A numerical study of inversion-layer breakup and the effects of topographic shading in idealized valleys. *J. Appl. Meteor.,* **42,** 1255–1272.

Dupont, S., and Y. Brunet, 2008: Influence of foliar density profile on canopy flow: A large-eddy simulation study. *Agric. For. Meteor.,* **148,** 976–990.

——, and ——, 2009: Coherent structures in canopy edge flow: A large-eddy simulation study. *J. Fluid Mech.,* **630,** 93–128.

Fast, J. D., and R. C. Easter, 2006: A Lagrangian particle dispersion model compatible with WRF. *Extended Abstracts, Seventh Annual WRF User's Workshop,* Boulder, CO, NCAR, P6.2. [Available online at http://www.mmm.ucar.edu/wrf/users/workshops/WS2006/WorkshopPapers.htm.]

Heilman, W. E., and Coauthors, 2013: Development of modeling tools for predicting smoke dispersion from low-intensity fires. Joint Fire Science Plan Study Final Rep. 09-1-04-1, 64 pp. [Available online at https://www.firescience.gov/projects/09-1-04-1/project/09-1-04-1_final_report.pdf.]

Janjić, Z. I., 1994: The step-mountain eta coordinate model: Further developments of the convection, viscous sublayer, and turbulence closure schemes. *Mon. Wea. Rev.,* **122,** 927–945.

Kain, J. S., and J. M. Fritsch, 1993: Convective parameterization for mesoscale models: The Kain–Fritsch scheme. *The Representation of Cumulus Convection in Numerical Models, Meteor. Monogr.,* No. 46, 165–170.

Kanda, M., and M. Hino, 1994: Organized structures in developing turbulent flow within and above a plant canopy, using a large eddy simulation. *Bound.-Layer Meteor.,* **68,** 237–257.

Keeley, J. E., 2009: Fire intensity, fire severity and burn severity: A brief review and suggested usage. *Int. J. Wildland Fire,* **18,** 116–126.

Kiefer, M. T., S. Zhong, W. E. Heilman, J. J. Charney, and X. Bian, 2013: Evaluation of an ARPS-based canopy flow modeling system for use in future operational smoke prediction efforts. *J. Geophys. Res.,* **118,** 6175–6188, doi:10.1002/jgrd.50491.

Larkin, N. K., and Coauthors, 2009: The BlueSky smoke modeling framework. *Int. J. Wildland Fire,* **18,** 906–920.

Lathrop, R. G., and M. B. Kaplan, 2004: New Jersey land use/land cover update to year 2000-2001. New Jersey Department of Environmental Protection, 35 pp. [Available online at http://www.nj.gov/dep/dsr/landuse/landuse00-01.pdf.]

Lavdas, L., 1996: Program VSMOKE—User's manual. USDA Forest Service General Tech. Rep. SRS-6, 156 pp. [Available online at http://www.srs.fs.usda.gov/pubs/1561.]

Lin, Y.-L., R. D. Farley, and H. D. Orville, 1983: Bulk parameterization of the snow field in a cloud model. *J. Appl. Meteor.,* **22,** 1065–1092.

Melvin, M. A., 2012: 2012 national prescribed fire use survey report. Coalition of Prescribed Fire Councils Inc. Tech. Rep. 01-12, 24 pp. [Available online at http://www.stateforesters.org/sites/default/files/publication-documents/2012_National_Prescribed_Fire_Survey.pdf.]

Mesinger, F., Z. I. Janjić, S. Nicković, D. Gavrilov, and D. G. Deaven, 1988: The step-mountain coordinate: Model description and performance for cases of Alpine lee cyclogenesis and for a case of an Appalachian redevelopment. *Mon. Wea. Rev.,* **116,** 1493–1518.

——, and Coauthors, 2006: North American Regional Reanalysis. *Bull. Amer. Meteor. Soc.,* **87,** 343–360.

Michioka, T., and F. K. Chow, 2008: High-resolution large-eddy simulations of scalar transport in atmospheric boundary layer flow over complex terrain. *J. Appl. Meteor. Climatol.,* **47,** 3150–3169.

Moeng, C.-H., and J. C. Wyngaard, 1989: Evaluation of turbulent transport and dissipation closures in second-order modeling. *J. Atmos. Sci.,* **46,** 2311–2330.

National Interagency Fire Center, cited 2012: Prescribed fire and acres by agency. [Available online at http://www.nifc.gov/fireInfo/fireInfo_stats_prescribed.html.]

Noilhan, J., and S. Planton, 1989: A simple parameterization of land surface processes for meteorological models. *Mon. Wea. Rev.,* **117,** 536–549.

Parker, M. D., and R. H. Johnson, 2004: Structures and dynamics of quasi-2D mesoscale convective systems. *J. Atmos. Sci.,* **61,** 545–567.

Patton, E. G., and Coauthors, 2011: The Canopy Horizontal Array Turbulence Study (CHATS). *Bull. Amer. Meteor. Soc.,* **92,** 593–611.

Pleim, J. E., and A. Xiu, 1995: Development and testing of a surface flux and planetary boundary layer model for application in mesoscale models. *J. Appl. Meteor.,* **34,** 16–32.

Raupach, M., and A. Thom, 1981: Turbulence in and above plant canopies. *Annu. Rev. Fluid Mech.,* **13,** 97–129.

Riebau, A. R., D. G. Fox, M. L. Sestak, B. Dailey, and S. F. Archer, 1988: Simple Approach Smoke Estimation Model. *Atmos. Environ.,* **22,** 783–788.

Seinfeld, J. H., 1975: *Air Pollution: Physical and Chemical Fundamentals.* McGraw-Hill, 523 pp.

Skowronski, N. S., K. L. Clark, M. Duveneck, and J. Hom, 2011: Three-dimensional canopy fuel loading predicted using upward and downward sensing LiDAR systems. *Remote Sens. Environ.,* **115,** 703–714, doi:10.1016/j.rse.2010.10.012.

Stohl, A., C. Forster, A. Frank, P. Seibert, and G. Wotawa, 2005: The Lagrangian particle dispersion model FLEXPART version 6.2. *Atmos. Chem. Phys.,* **5,** 2461–2474.

Sun, H., T. L. Clark, R. B. Stull, and T. A. Black, 2006a: Two-dimensional simulation of airflow and carbon dioxide transport over a forested mountain. Part I: Interactions between thermally-forced circulations. *Agric. For. Meteor.,* **140,** 338–351.

Sun, R., M. A. Jenkins, S. K. Krueger, W. Mell, and J. J. Charney, 2006b: An evaluation of fire-plume properties simulated with the Fire Dynamics Simulator (FDS) and the Clark coupled wildfire model. *Can. J. For. Res.,* **36,** 2894–2908.

Sun, W.-Y., and C.-Z. Chang, 1986: Diffusion model for a convective layer: Part I: Numerical simulation of convective boundary layer. *J. Climate Appl. Meteor.,* **25,** 1445–1453.

Sun, X.-M., Z.-L. Zhu, X.-F. Wen, G.-F. Yuan, and G.-R. Yu, 2006c: The impact of averaging period on eddy fluxes observed at ChinaFLUX sites. *Agric. For. Meteor.,* **137,** 188–193.

Xue, M., K. K. Droegemeier, and V. Wong, 2000: The Advanced Regional Prediction System (ARPS)—A multi-scale nonhydrostatic atmosphere simulation and prediction model. Part I: Model dynamics and verification. *Meteor. Atmos. Phys.,* **75,** 463–485.

——, and Coauthors, 2001: The Advanced Regional Prediction System (ARPS)—A multi-scale nonhydrostatic atmosphere simulation and prediction tool. Part II: Model physics and applications. *Meteor. Atmos. Phys.,* **76,** 143–165.

——, D. Wang, J. Gao, K. Brewster, and K. K. Droegemeier, 2003: The Advanced Regional Prediction System (ARPS), storm-scale numerical weather prediction and data assimilation. *Meteor. Atmos. Phys.,* **82,** 139–170.